The Astrophysical Journal, 820:101 (13pp), 2016 April 1 doi:10.3847/0004-637X/820/2/101

PECULIAR VELOCITY CONSTRAINTS FROM FIVE-BAND SZ EFFECT MEASUREMENTS TOWARD RX J1347.5−1145 WITH MUSIC AND BOLOCAM FROM THE CSO

Jack Sayers[1], Michael Zemcov[2], Jason Glenn[3], Sunil R. Golwala[1], Philip R. Maloney[3], Seth R. Siegel[1], Jordan Wheeler[3], Clint Bockstiegel[4], Spencer Brugger[3], Nicole G. Czakon[5], Peter K. Day[6], Thomas P. Downes[7], Ran P. Duan[8], Jiansong Gao[9], Matthew I. Hollister[1], Albert Lam[1], Henry G. LeDuc[6], Benjamin A. Mazin[4], Sean G. McHugh[4], David A. Miller[1], Tony K. Mroczkowski[10,12], Omid Noroozian[11], Hien T. Nguyen[6], Simon J. E. Radford[1], James A. Schlaerth[1,3], Anastasios Vayonakis[1], Philip R. Wilson[6], and Jonas Zmuidzinas[1]
[1] Division of Physics, Math, and Astronomy, California Institute of Technology, Pasadena, CA 91125, USA; jack@caltech.edu
[2] Rochester Institute of Technology, Rochester, NY 14623, USA
[3] Department of Astrophysical and Planetary Science, University of Colorado, Boulder, CO 80309, USA
[4] Department of Physics, University of California, Santa Barbara, CA 93106, USA
[5] Institute of Astronomy and Astrophysics, Academia Sinica, Taipei, Taiwan
[6] Jet Propulsion Laboratory, Pasadena, CA 91109, USA
[7] Department of Physics, University of Wisconsin, Milwaukee, WI 53201, USA
[8] National Astronomical Observatories, Chinese Academy of Sciences, Chaoyang District, Beijing, China
[9] National Institute of Standards and Technology, Boulder, CO 80305, USA
[10] United States Naval Research Laboratory, Washington, DC 20375, USA
[11] Goddard Space Flight Center, Greenbelt, MD 20771, USA
Received 2015 September 9; accepted 2016 February 20; published 2016 March 24

ABSTRACT

We present Sunyaev-Zel'dovich (SZ) effect measurements from wide-field images toward the galaxy cluster RX J1347.5−1145 obtained from the Caltech Submillimeter Observatory with the Multiwavelength Submillimeter Inductance Camera at 147, 213, 281, and 337 GHz and with Bolocam at 140 GHz. As part of our analysis, we have used higher frequency data from *Herschel*–SPIRE and previously published lower frequency radio data to subtract the signal from the brightest dusty star-forming galaxies behind RX J1347.5−1145 and from the AGN in RX J1347.5−1145's BCG. Using these five-band SZ effect images, combined with X-ray spectroscopic measurements of the temperature of the intra-cluster medium (ICM) from *Chandra*, we constrain the ICM optical depth to be $\tau_e = 7.33^{+0.96}_{-0.97} \times 10^{-3}$ and the ICM line of sight peculiar velocity to be $v_{pec} = -1040^{+870}_{-840}$ km s^{-1}. The errors for both quantities are limited by measurement noise rather than calibration uncertainties or astrophysical contamination, and significant improvements are possible with deeper observations. Our best-fit velocity is in good agreement with one previously published SZ effect analysis and in mild tension with the other, although some or all of that tension may be because that measurement samples a much smaller cluster volume. Furthermore, our best-fit optical depth implies a gas mass slightly larger than the *Chandra*-derived value, implying the cluster is elongated along the line of sight.

Key words: galaxies: clusters: individual: (RX J1347.5−1145) – galaxies: clusters: intracluster medium

1. INTRODUCTION

The peculiar velocities (v_{pec}) of galaxy clusters and other large-scale structures are related to the underlying cosmology, particularly the properties of dark energy and the long length-scale behavior of gravity. As such, measurements of v_{pec} can be used to place constraints on a variety of cosmological parameters (e.g., Kaiser 1987; Scoccimarro 2004; Bhattacharya & Kosowsky 2008; Kosowsky & Bhattacharya 2009). In addition, the assumption of large-scale homogeneity in the universe based on the Copernican principle can also be tested using v_{pec} measurements (Clarkson et al. 2008; Clarkson 2012; Planck Collaboration et al. 2014). The kinetic Sunyaev-Zel'dovich (SZ) effect, which describes the Doppler shift of Cosmic Microwave Background (CMB) photons that scatter off of hot electrons in the intra-cluster medium (ICM), provides an excellent tool for such measurements (Sunyaev & Zel'dovich 1972; Birkinshaw 1999; Carlstrom et al. 2002; Sunyaev & Zel'dovich 1980). In particular, the surface brightness of the kinetic SZ effect signal is independent of redshift and is directly proportional to the line of sight peculiar velocity of the ICM relative to the fixed reference frame of the CMB.

However, the relative dimness of the kinetic SZ effect signal, along with contamination from several other astrophysical sources such as primary CMB fluctuations and the thermal SZ effect, present a significant observational challenge. Recently, progress has been made by averaging the kinetic SZ effect signal over large samples of objects in wide field CMB surveys. For example, kinetic SZ effect measurements based on multi-band data from the *WMAP* and *Planck* satellites have been used to place upper limits on the average and rms peculiar velocities of large (≃1000) X-ray selected cluster samples (Kashlinsky et al. 2008; Osborne et al. 2011; Planck Collaboration et al. 2014). In addition, *Planck* and the ground-based Atacama Cosmology Telescope (ACT) have made separate modest-significance detections of the kinetic SZ effect signal using pairwise stacks on galaxies detected in the Sloan Digital Sky Survey (Hand et al. 2012; Planck Collaboration et al. 2015a). Furthermore, data from *Planck*, ACT, and the ground-based South Pole Telescope imply a non-zero kinetic SZ effect power spectrum on small angular scales (Sievers et al. 2013; George et al. 2015; Planck Collaboration et al. 2015b). Complementary

[12] National Research Council Fellow.

to these large statistical analyses, several efforts have also been made to detect the kinetic SZ effect signal in individual clusters using multi-band ground-based measurements (Benson et al. 2003; Kitayama et al. 2004; Mauskopf et al. 2012; Mroczkowski et al. 2012; Zemcov et al. 2012; Adam et al. 2015; Lindner et al. 2015), with an exceptionally high velocity merging component in the cluster MACS J0717.5+3745 producing the highest significance detection to date (Sayers et al. 2013c).

This analysis focuses on SZ effect measurements toward the cluster RX J1347.5−1145, which is a well-studied system that was the target of some of the earliest published thermal SZ effect detections (Komatsu et al. 1999; Pointecouteau et al. 1999; Komatsu et al. 2001; Pointecouteau et al. 2001; Reese et al. 2002). Due to its brightness, RX J1347.5−1145 has also been used for the initial studies published from several recent SZ effect instruments (Mason et al. 2010; Zemcov et al. 2012; Adam et al. 2014). In addition, two separate kinetic SZ effect measurements toward RX J1347.5−1145 have been published. Kitayama et al. (2004) found $v_{\rm pec} = -1420^{+1170}_{-1270}$ km s^{-1} based on 21, 150, and 350 GHz measurements collected from the Nobeyama 45 m Radio Telescope and the James Clerk Maxwell Telescope, and Zemcov et al. (2012) used high spectral resolution 200–300 GHz data from Z-Spec combined with 140 GHz Bolocam data to constrain $v_{\rm pec} = +450 \pm 810$ km s^{-1}.[13]

In this manuscript we present SZ effect measurements toward RX J1347.5−1145 that were collected at 147, 213, 281, and 337 GHz using the Multiwavelength Submillimeter Inductance Camera (MUSIC) and at 140 GHz with Bolocam. Summaries of the instrument characteristics are given in Section 2, and the data reduction procedures are described in Section 3. Section 4 details the analysis of *Chandra* X-ray exposures to obtain a spectroscopic constraint on the ICM temperature $T_{\rm e}$. Section 5 discusses the model used to describe the shape of the SZ effect signal toward RX J1347.5−1145, and Section 6 details how the SZ brightness measurements derived from the model fits, in combination with the X-ray spectroscopic measurements, are used to constrain the ICM optical depth $\tau_{\rm e}$ and peculiar velocity $v_{\rm pec}$. A comparison to previously published results is given in Section 7. Throughout this manuscript, all physical quantities have been derived using a flat cosmology with $\Omega_{\rm M} = 0.3$, $\Omega_\lambda = 0.7$, and $H_0 = 70$ km s^{-1} Mpc^{-1}.

2. SZ EFFECT INSTRUMENTATION

2.1. MUSIC

MUSIC was built to serve as the long-wavelength imaging camera for the Caltech Submillimeter Observatory (CSO), and its overall design and construction are detailed in Glenn et al. (2008), Maloney et al. (2010), Golwala et al. (2012), and Sayers et al. (2014). Relative to the instrument description in Sayers et al. (2014), the cryogenic lens has been redesigned in order to change the plate scale of the focal plane from 7″ mm^{-1} to 11.″5 mm^{-1}. As originally built, eight focal plane tiles would fill MUSIC's 14′ circular field of view (FOV). However, the initial fabrication yielded only two working tiles, and this plate scale change allows these two tiles to fill a square 11.′5 FOV (14′ diagonal). Subsequent to this redesign, one of the working tiles was damaged, and all of the data described in this manuscript were collected using a single tile with an approximate FOV of 5.′8 × 11.′5 (AZ × EL).

The MUSIC focal plane uses phased arrays of slot antennas to couple to incoming radiation over a broad bandwidth spanning from ≃100–400 GHz (Goldin et al. 2003). The output from each antenna array is then coupled to four separate microwave kinetic inductance detectors (MKIDs), with three-pole lumped element filters defining a different observing band for each MKID (Kumar et al. 2009; Duan 2015). These four observing bands are centered at 147, 213, 281, and 337 GHz,[14] and they have corresponding point spread functions (PSFs) that are approximately Gaussian and have full-width half maxima (FWHM) of 48″, 36″, 32″, and 29″.[15] Each MUSIC focal plane tile consists of 72 antenna arrays and 288 MKIDs, and the tile used to collect the data described in this manuscript has 200 MKIDs that pass all of the initial quality checks. An additional cut is made based on the on-sky sensitivity of each detector, removing all MKIDs with a sensitivity more than two standard deviations poorer than the median sensitivity within each observing band. After this cut 125 MKIDs remain, with 30, 35, 32, and 28 MKIDs at 147, 213, 281, and 337 GHz.

2.2. Bolocam

Bolocam served as the long-wavelength imaging camera at the CSO prior to the installation of MUSIC, and the instrument is described in detail in Glenn et al. (1998) and Haig et al. (2004). Bolocam operated with an 8′ circular FOV filled with 144 spiderweb bolometers using neutron-transmutation-doped Ge thermistors, of which approximately 115 were optically coupled. The data described in this manuscript were collected with Bolocam operating at 140 GHz, where the PSFs had a FWHM of 58″.

As detailed in Section 6, the Bolocam data provide a modest improvement in constraining the SZ effect signal compared to using the MUSIC data alone. In addition, this is the first SZ analysis using MUSIC data, while the Bolocam data for RX J1347.5−1145 have already been published in multiple analyses (e.g., Sayers et al. 2013b, 2013a; Czakon et al. 2015). As a result, the well-vetted Bolocam data provide a useful consistency check for the MUSIC measurements.

3. SZ DATA REDUCTION

3.1. General Reduction and Calibration

For both MUSIC and Bolocam, the data were collected by scanning the CSO in a Lissajous pattern with an rms speed of 240″ s^{-1} and an amplitude of 3′ and 4′, respectively. Nightly observations of Uranus or Neptune were made to determine the absolute flux calibration of the data, which is estimated to have an rms uncertainty of 5.0% for Bolocam and 6.0%, 4.6%, 5.5%, and 9.4% in the 147, 213, 281, and 337 GHz MUSIC observing bands (Sayers et al. 2013a; Sayers et al. 2014). Included in all of the above uncertainties is an overall 3.3% rms uncertainty in the normalization of the planetary brightness model (Sayers et al. 2012). In the case of Bolocam, hourly observations of bright compact objects were made in order to obtain a pointing accuracy of ≃5″ rms (Sayers et al. 2011). For

[13] Kitayama et al. (2004) report a value of +1420 km s^{-1}, but that value is based on an opposite convention for the velocity direction compared to what is used in this work and in Zemcov et al. (2012).

[14] These values represent the effective band centers for a relativistically corrected thermal SZ spectrum assuming an ICM temperature of 10 keV.

[15] These FWHM are slightly larger than the values given in Sayers et al. (2014) due to the optical reconfiguration.

Table 1
Bolocam+MUSIC Data

band (GHz)	PSF	HPF (Half-signal)	HPF ($2\times R_{2500}$)	rms/beam	Image Size
140 GHz	$58''$	$(9'.5)^{-1}$	0.89	1.1 mJy	$14' \times 14'$
147 GHz	$48''$	$(2'.5)^{-1}$	0.30	1.1 mJy	$12' \times 12'$
213 GHz	$36''$	$(2'.4)^{-1}$	0.26	0.8 mJy	$12' \times 12'$
281 GHz	$32''$	$(2'.9)^{-1}$	0.33	2.0 mJy	$12' \times 12'$
337 GHz	$29''$	$(2'.7)^{-1}$	0.29	7.2 mJy	$12' \times 12'$

Note. The Bolocam+MUSIC data used in this analysis. The columns give the thermal SZ effect-weighted band center, the PSF FWHM, the angular scale at which half of the signal from a cluster-sized object is attenuated due to the effective high-pass filtering of the data processing, the fraction of signal remaining for angular scales corresponding to $2 \times R_{2500} = 4'.1$ (see Section 5), the rms/beam in the image, and the total size of the image.

MUSIC, a single pointing offset derived from the flux calibration observations is sufficient to obtain a pointing accuracy of $\simeq 3''$ rms, and therefore no dedicated observations were made for the purpose of pointing calibration (Sayers et al. 2014).

The Bolocam data have been used in several SZ effect analyses, and the details of their reduction are described in Sayers et al. (2011, 2013a), and Czakon et al. (2015). Briefly, a template for the atmospheric brightness fluctuations is formed from the average bolometer signal at each time sample. This template is then correlated and regressed from each bolometer's time-ordered data (TOD). Next, a high-pass filter with a characteristic frequency of 250 mHz is applied to the TOD. Both of these processes attenuate SZ effect signal, and an image-space transfer function is computed by reverse-mapping and processing a cluster model through the same reduction pipeline. See Table 1.

In order to reduce the MUSIC data, the first step is to locate discontinuous jumps in the TOD that appear to be caused by the readout electronics. When a discontinuity is found, the TOD for that MKID is flagged and removed from the entire 10-minute long observation. In total, approximately 10% of the data are flagged. The MUSIC instrument moves along with the CSO telescope during the Lissajous scans, and this motion relative to the Earth's magnetic field produces a response in the MKIDs at the level of $\simeq 10$ mJy peak-to-peak. To remove this response, templates of the AZ and EL motion of the telescope are correlated and regressed from the resonant-frequency-response TOD of each MKID (changing magnetic fields do not produce a signal in the dissipation-response TOD).[16] Additional noise fluctuations, with $1/f$ and $1/f^2$ power spectra, are sourced by gain and phase fluctuations in the MUSIC readout electronics. Templates for these fluctuations are constructed from electronics fluctuation monitors and then subtracted from the MKID TODs. Analogous to the Bolocam analysis procedure, a template of the atmospheric brightness fluctuations is then subtracted, with a separate template constructed for each of the four observing bands. A high-pass filter with a characteristic frequency of 500 mHz is then applied to the TOD. Compared to Bolocam, the MUSIC data contain more low-frequency noise due to both residual instrumental and atmospheric noise, and therefore a more aggressive high-pass filter provides an improved signal-to-noise ratio in the MUSIC data. Finally, the overall image-space transfer function of the MUSIC processing is determined separately for each observing band using the same procedure as for Bolocam. Due to MUSIC's slightly smaller FOV, along with the higher frequency high-pass filter applied to the MUSIC TOD, the Bolocam images retain fidelity to cluster emission on larger angular scales than the MUSIC images. See Table 1.

[16] The MUSIC readout works by using a single probe tone centered on the nominal resonant frequency of each MKID (Duan et al. 2010). Changes in the resonance depth and/or frequency thus produce a change in the complex-valued transmission of this probe tone. A full calibration sweep of the resonance is performed once every 30 minutes, and this sweep provides a mapping from the complex-valued TOD to separate real-valued TODs that represent the change in the resonance frequency and resonance depth (or dissipation). For MUSIC, the signal-to-noise for astronomical sources is many times larger in the frequency response than in the dissipation response, and so the dissipation-response TODs are not used in this analysis.

3.2. Point Source Subtraction

The BCG of RX J1347.5−1145 hosts a strong AGN, and its emission is non-negligible compared to the SZ effect signal in the Bolocam+MUSIC observing bands. Due to Bolocam +MUSIC's relatively coarse angular resolution, and the fact that the AGN is spatially coincident with the peak in the SZ effect signal, it is not possible to model and subtract the AGN emission using Bolocam+MUSIC data alone. As a result, a wide range of available measurements of the AGN at frequencies close to the Bolocam+MUSIC observing bands were used to obtain a power-law fit to the flux density of the AGN. Specifically, these data include a 1.4 GHz measurement from NVSS (Condon et al. 1998), 8.5 and 22.5 GHz measurements from VLA (Komatsu et al. 2001), a 28.5 GHz measurement from OVRO/BIMA (Coble et al. 2007), a 30.9 GHz measurement from SZA (Bonamente et al. 2012), a 90 GHz measurement from MUSTANG (Korngut et al. 2011), 86 and 90 GHz measurements from CARMA (Plagge et al. 2013), a 100 GHz measurement from NMA (Komatsu et al. 1999), a 140 GHz measurement from Diablo (Pointecouteau et al. 2001), and a 250 GHz measurement from SCUBA (Komatsu et al. 1999). All of these data were collected using interferometers except for MUSTANG (which is a high angular-resolution single-dish photometer), Diablo (where the SZ effect and AGN signals were simultaneously modeled), and SCUBA (which was relatively close to the null in the thermal SZ effect signal). See Figure 1. The best fit obtained using LINMIX_ERR (Kelly 2007), which accounts for intrinsic scatter between measurements due to potential, unaccounted-for instrumental systematics and/or source variability, is

$$F(\nu) = (59.1\ \mathrm{mJy}) \times \left(\frac{\nu}{\mathrm{GHz}}\right)^{-0.527}.$$

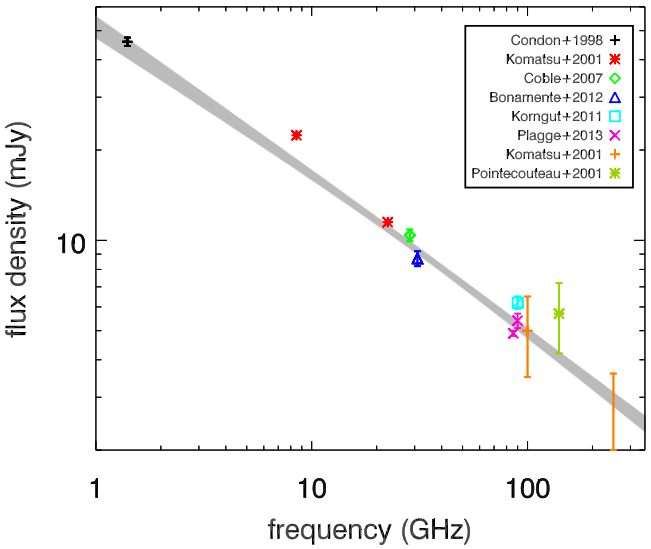

Figure 1. Measurements of the flux density of the AGN in the BCG of RX J1347.5−1145 at frequencies close to the Bolocam+MUSIC observing bands (see the text for more details). Overlaid in gray is the 68% confidence region for a power-law fit obtained using LINMIX_ERR. This fit has a fractional uncertainty of 10% at the frequencies corresponding to the Bolocam+MUSIC bands at 140–337 GHz.

Extrapolating this fit to the Bolocam+MUSIC observing bands yields flux densities of 4.37, 4.26, 3.50, 3.03, and 2.75 mJy at 140, 147, 213, 281, and 337 GHz. Rounded to the nearest percent, the rms uncertainty on the extrapolation is 10% in all of the Bolocam+MUSIC observing bands, and this uncertainty is included in the noise estimates as described in Section 3.3 below.

In addition to the BCG, the Bolocam+MUSIC images also contain a non-negligible signal from the population of dusty star-forming galaxies behind RX J1347.5−1145, although none of these galaxies are individually detected at high significance in the Bolocam+MUSIC data. The emission from these sources has been subtracted according to the general procedure described in detail in the Appendix of Sayers et al. (2013c) with some slight modifications described below. Briefly, a list of candidate galaxies is compiled from the three-band *Herschel*–SPIRE observations at 600, 850, and 1200 GHz. In total, 192 galaxy candidates are detected by *Herschel*–SPIRE, with a signal-to-noise above 3 in at least one of the *Herschel*–SPIRE bands. For each galaxy candidate, a graybody spectrum is fit to the *Herschel*–SPIRE measurements and is extrapolated to the Bolocam+MUSIC observing bands. For each band, the source positions and brightness estimates for all of the galaxies are combined into a single model of the background galaxy emission. Next, these models are fit to the Bolocam+MUSIC data, floating the value of the overall normalization separately for each observing band (see Table 2). The average normalization over the five bands is 1.36 ± 0.23, indicating that the background emission from the star-forming galaxies is slightly brighter than the graybody extrapolation in the Bolocam+MUSIC bands. Therefore, the *Herschel*–SPIRE model is multiplied by a factor of 1.36 prior to subtracting it from the Bolocam+MUSIC data, and the rms uncertainty on this scaling factor is taken to be 0.23 (see Section 3.3).

Table 2
Herschel–SPIRE Dusty Star-forming Galaxy Model

Band (GHz)	140	147	213	281	337	Total
Normalization	−0.73	2.27	1.47	1.12	2.24	1.36
Uncertainty	1.53	1.58	0.34	0.36	0.80	0.23

Note. Bolocam+MUSIC-derived fits to the normalization of the dusty star-forming galaxy model obtained from *Herschel*–SPIRE. Averaging all four bands together, a best-fit normalization of 1.36 ± 0.23 is obtained, indicating that the emission in the Bolocam+MUSIC observing bands is 36% brighter than the *Herschel*–SPIRE graybody extrapolation.

Although a single scaling factor for the *Herschel*–SPIRE model is assumed for all five Bolocam+MUSIC observing bands, it is possible that the slight mismatch between the graybody extrapolation and the Bolocam+MUSIC data is due to the assumed graybody shape rather than the overall normalization. However, the Bolocam+MUSIC measurements are not precise enough to distinguish between the two scenarios, and so the simpler case of an overall normalization factor is used for this analysis. Furthermore, as described in Section 6, the extreme case of not subtracting any model of the dusty star-forming galaxies results in only modest changes to the derived ICM constraints, and consequently any minor differences between the assumed and true graybody models are unlikely to have a significant impact on the overall results.

Images of the Bolocam+MUSIC data, along with the background dusty star-forming galaxy and AGN models, are shown in Figure 2. The potential impact of these point sources on the SZ effect constraints is explored in more detail in Section 6.

3.3. Noise Estimation

The Bolocam+MUSIC data contain noise from several different sources, including the instruments themselves, the random arrival of photons, the atmosphere, and the astronomical sky. In all cases, the noise is characterized by a set of 1000 separate five-band image realizations that are used to construct a noise covariance matrix in a bootstrap fashion (see Section 5). Some of the noise in each of the 1000 realizations is correlated between the separate bands, and therefore a single noise realization contains images for all five bands. Each of these noise realizations is constructed as described below, and the effects of each noise source on constraining the SZ effect signal are detailed in Section 5.

1. Instrument, photon, and atmosphere: a jackknife image is formed by multiplying the data in a randomly selected subset of half the observations by −1 prior to producing the image. This jackknife preserves the noise properties of the instrument, random photon, and atmospheric brightness fluctuations, including correlations between observing bands, but it removes all astronomical signals. This is the dominant noise in the data, particularly in the four MUSIC bands.
2. AGN: the template image of the AGN is different for each observing band, and consists of that band's PSF,

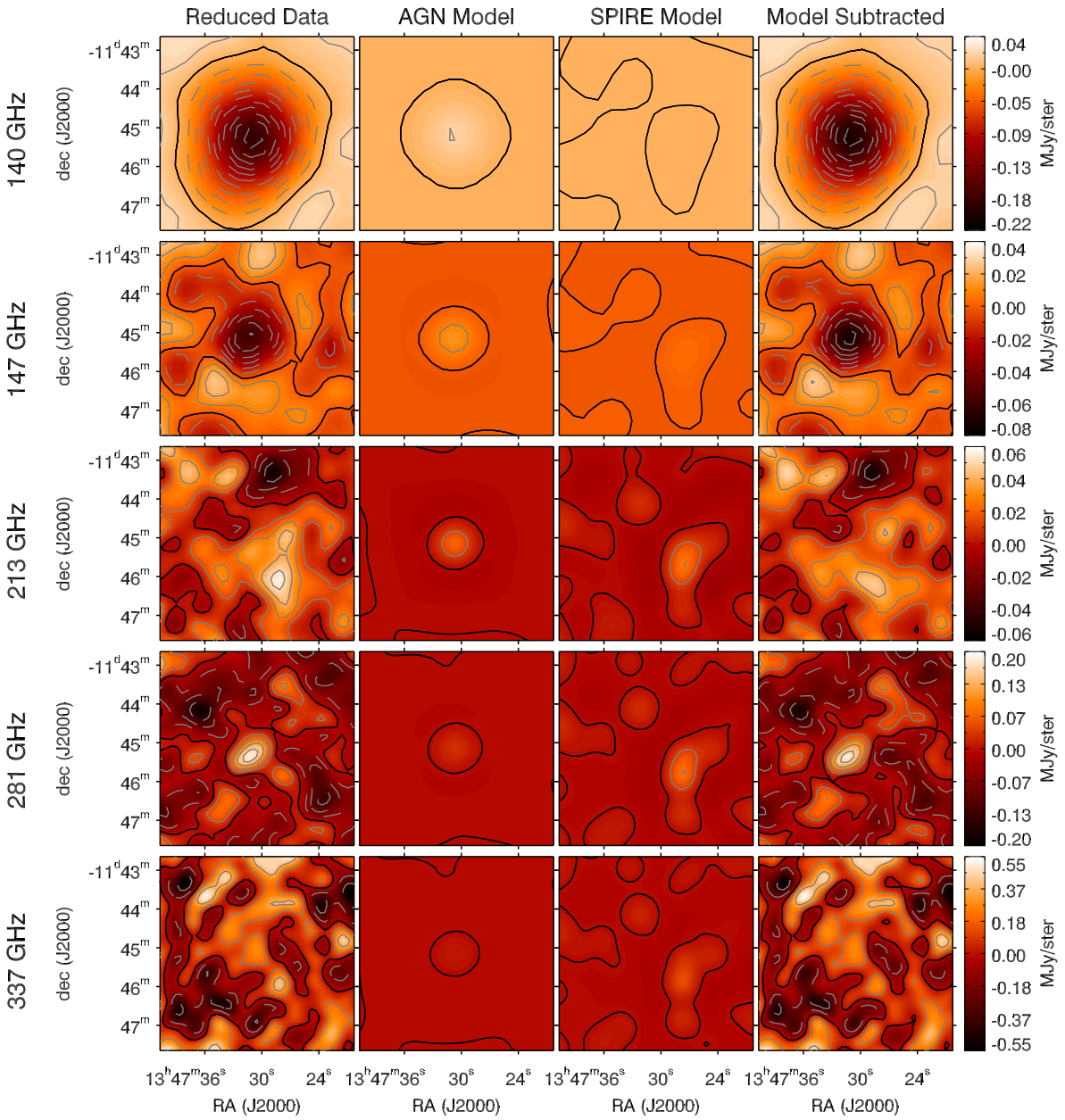

Figure 2. From left to right the columns show thumbnails of the Bolocam+MUSIC data, the model of the AGN emission from the cluster BCG, the *Herschel*–SPIRE-derived model for the brightest dusty star-forming galaxies, and the Bolocam+MUSIC data after subtracting both of these models. For MUSIC, the solid gray lines show positive S/N in steps of 1, and the dashed gray lines show negative S/N in steps of 1 (for Bolocam the lines indicate steps of ±3). The solid black line is at 0. In all cases, the color scale has been stretched to cover the maximum and minimum image values. All of the images have been filtered, and the more aggressive high-pass filter applied to the MUSIC data results in a more compact size for the SZ effect signal compared to the Bolocam data.

after accounting for the filtering effects of the data processing, multiplied by the estimated flux density of the AGN in that band. Based on the fit presented in Section 3.2, a 10% rms uncertainty was assigned to the estimated flux density of the AGN. Furthermore, because any fractional deviation in the source brightness from the model will be common among all five Bolocam+MUSIC observing bands, the noise fluctuations are assumed to be completely correlated between the five observing bands. Specifically, the AGN template in the five bands is multiplied by a single, common Gaussian random value drawn from a distribution with a mean of 1.0 and a standard deviation of 0.1.

3. *Herschel*–SPIRE-detected galaxies: the normalization of the *Herschel*–SPIRE-derived model was determined to be 1.36 ± 0.23, and a Gaussian random value based on this constraint is used to describe the uncertainty on this model. For each observing band, a template is constructed based on the *Herschel*–SPIRE model and that band's PSF and data processing filter. As with the AGN template, the noise fluctuations are assumed to be completely correlated between all five observing bands due to the fact that a fractional change in source brightness in one band will result in the same fractional change in the other four bands given the nominal graybody fit.

4. Undetected dusty star-forming galaxies: although *Herschel*–SPIRE detects 192 galaxy candidates toward RX J1347.5−1145, the bulk of the population of dusty star-forming galaxies is below the *Herschel*–SPIRE detection limit. In order to account for brightness fluctuations due to the non-uniform spatial distribution of these galaxies, a random sky realization is generated based on the model of Béthermin et al. (2011), after correcting the model for the galaxies that were detected by *Herschel*–SPIRE and subtracted (see the Appendix of Sayers et al. (2013c) for more details). A single sky realization is used for all five observing bands in order to preserve the correlations between bands. For each band, the sky realization is convolved with the PSF and data processing filter.
5. Primary CMB fluctuations: a random sky realization is generated based on the power spectrum measurements from Planck Collaboration et al. (2015b) and is added to the noise realizations for each of the five observing bands after correcting for each band's PSF and data-processing filter. As with the sky realizations of the undetected dusty star-forming galaxies, a single sky realization is used for all five bands in order to preserve the correlations between bands.
6. Flux calibration: the flux calibration uncertainty includes two separate components. The overall planetary brightness model has an uncertainty of 3.3%, and fluctuations based on this uncertainty are assumed to be completely correlated between all five observing bands. In addition, as described in Section 3.1, there is an uncorrelated measurement uncertainty on the flux calibration for each observing band.

4. X-RAY DATA REDUCTION

As described below in Section 6, a *Chandra* X-ray constraint on the ICM temperature T_e is included in the overall analysis. This measurement of T_e was obtained from the longest *Chandra* observation of RX J1347.5−1145, ID 14407, which was reprocessed using CIAO version 4.7 (2014 December) and CALDB 4.6.9 (2015 September). The observation is very clean, with 62.9 ks from the 63.2 ks exposure remaining after light curve filtering to reject any 200-second bins where the count rate varied by more than 3σ from the median. The standard ACIS background file was scaled to match the off-source count rate in the 10–12 keV energy range, and subtracted. Spectral fits were performed with the 0.7–9.5 keV band using a photon-absorbed APEC plasma model with $n_H = 4.60 \times 10^{20}$ cm^2 (the Leiden–Argentine–Bonn value for RX J1347.5−1145's sky position). Excising the extremely bright cool-core at a radius of 150 kpc (0.′43) results in an emission-weighted $T_e = 13.4 \pm 0.7$ keV within R_{2500}. This measurement differs somewhat compared to previous X-ray measurements of T_e. For example, Mahdavi et al. 2013 find $T_e = 12.1 \pm 0.4$ keV based on a combined *Chandra–XMM* analysis. Furthermore, there is substantial evidence that the ICM is not isothermal within R_{2500} (e.g., Johnson et al. 2012). Section 6 explores the impact of these different T_e values on the overall ICM constraints.

Table 3
gNFW Model Fit Parameters

Instrument	Band (GHz)	p_0 (10^{-11} erg cm^{-3})	χ^2/DOF	PTE
Bolocam	140	34.3 ± 1.5	147/118	0.04
MUSIC	147	28.6 ± 4.0	239/206	0.06
MUSIC	213	−16.6 ± 26.9	456/466	0.62
MUSIC	281	38.6 ± 11.2	740/730	0.39
MUSIC	337	24.8 ± 26.4	919/971	0.88

Note. Summary of the gNFW model fits to MUSIC and Bolocam. The shape of the model is based on the fit published in Table 2 of Czakon et al. (2015), and the only free parameter in the fits is the normalization of the model p_0. In the limit of a purely thermal SZ signal, the value of p_0 will be the same for all five observing bands. Except for the 213 GHz band, which is near the thermal SZ effect null and easily contaminated by the kinetic SZ effect signal, there is good agreement between the MUSIC and Bolocam measurements. In addition, the quality of fit in all five bands is good, indicating that the data are consistent with the assumed model. The PTE values are based on the theoretical χ^2 distribution, and therefore may be slightly biased (see Tables 2 and 3 in Sayers et al. 2011).

5. SPATIAL MODEL OF THE SZ EFFECT SIGNAL

Although RX J1347.5−1145 shows evidence for a shock in the ICM to the SE of the cluster core (Mason et al. 2010; Johnson et al. 2012; Kreisch et al. 2014), its X-ray morphology indicates that it is among the most relaxed known clusters (Mantz et al. 2015). As a result, the best-fit elliptical generalized Navarro, Frenk, and White (gNFW, Nagai et al. 2007) profile from Table 2 of Czakon et al. (2015), based on a fit to the Bolocam data, was selected to model the spatial shape of the SZ effect signal. This spatial template was then convolved with the PSF and data-processing filter specific to each of the five observing bands. The normalization of the template was varied as a free parameter separately for each observing band using all of the data within the overdensity radius $R_{2500} = 0.71$ Mpc (2.′05) published in Czakon et al. (2015) based on the techniques described in Mantz et al. (2010).[17] This model produces a good fit quality in all five observing bands, as quantified in Table 3 and shown in the thumbnails in Figure 3 and the radial profiles in Figure 4. Based on these model fits, the average SZ effect brightness within R_{2500} was computed for each band, with the results given in Table 4.

In performing the model fits, the image pixel weighting and overall χ^2 values were computed based on the assumption that the noise is uncorrelated between pixels. Specifically, the image-space pixel sensitivity was computed for each observing band based on the standard deviation of the pixel flux density weighted by the square root of integration time in the set of 1000 noise realizations described in detail in Section 3.3. This assumption is not strictly correct, as many of the noise terms are correlated between image pixels and between observing bands. Therefore, to fully account for the noise, the spatial template of the SZ effect signal was also fit to each of the 1000 noise realizations and these fits were used to

[17] R_{2500} is the radius enclosing an average density 2500 times the critical density of the universe. As shown in Table 1, the Bolocam+MUSIC data have good sensitivity to angular scales corresponding to R_{2500}, allowing for accurate constraints within that aperture size.

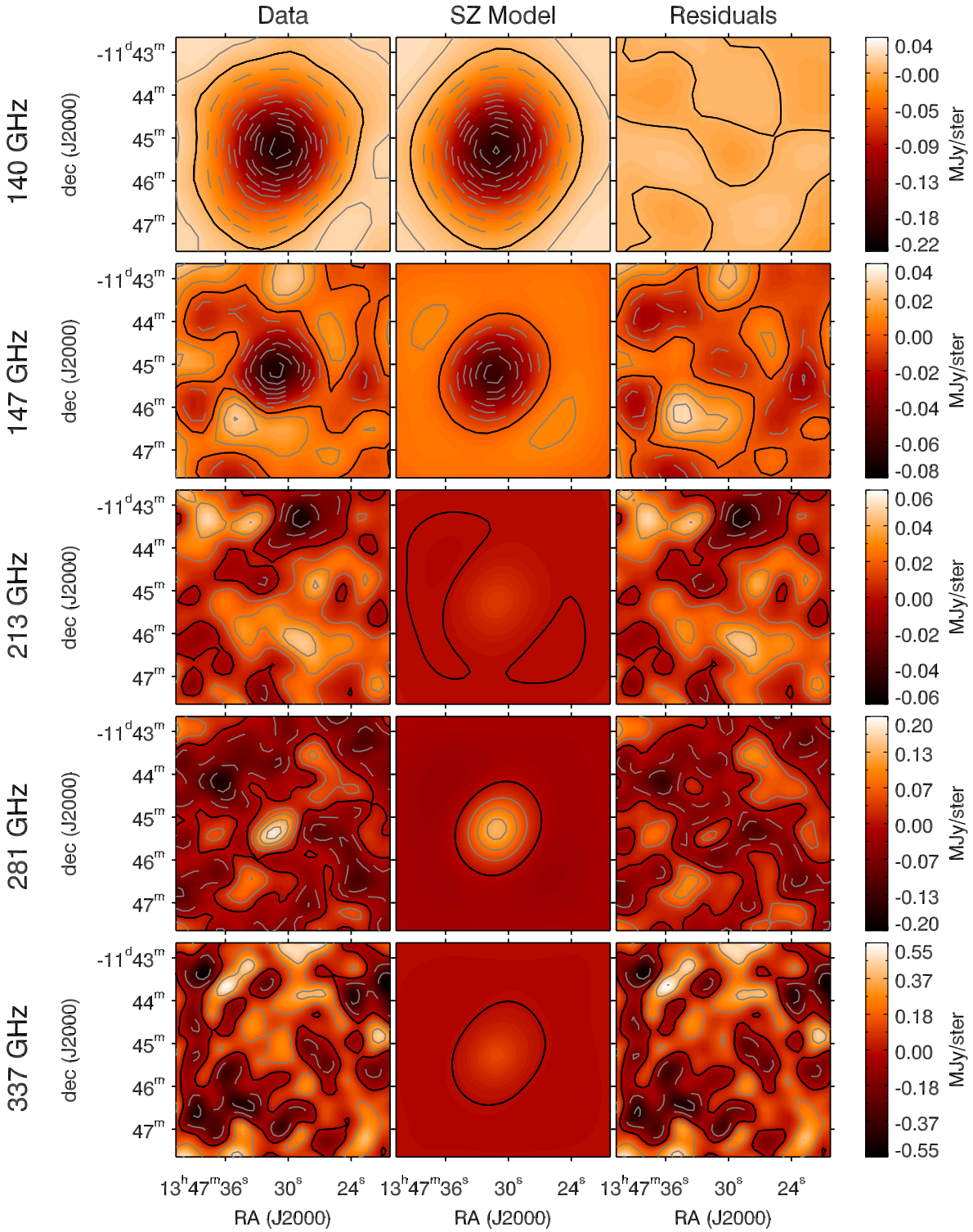

Figure 3. From left to right the columns show thumbnails of the Bolocam+MUSIC data after subtracting the AGN and dusty star-forming galaxy model, the best-fit model of the SZ effect signal based on the elliptical gNFW model from Table 2 of Czakon et al. (2015), and the residuals after subtracting the SZ effect model. In all cases, the SZ effect model provides a good fit to the data, and the residuals are consistent with noise.

compute the full 5 × 5 covariance matrix for the SZ effect brightness. The covariance matrix is given in Table 4 and the relative contributions of the noise terms described in Section 3.3 to this covariance matrix are plotted in Figure 5. Many of the off-diagonal elements of the SZ effect brightness covariance matrix are comparable in magnitude to the on-diagonal elements, particularly for adjacent observing bands. In the case of MUSIC, which obtains simultaneous multi-band images, some of this correlation is due to fluctuations in the atmospheric brightness. However, the bulk of the band-to-

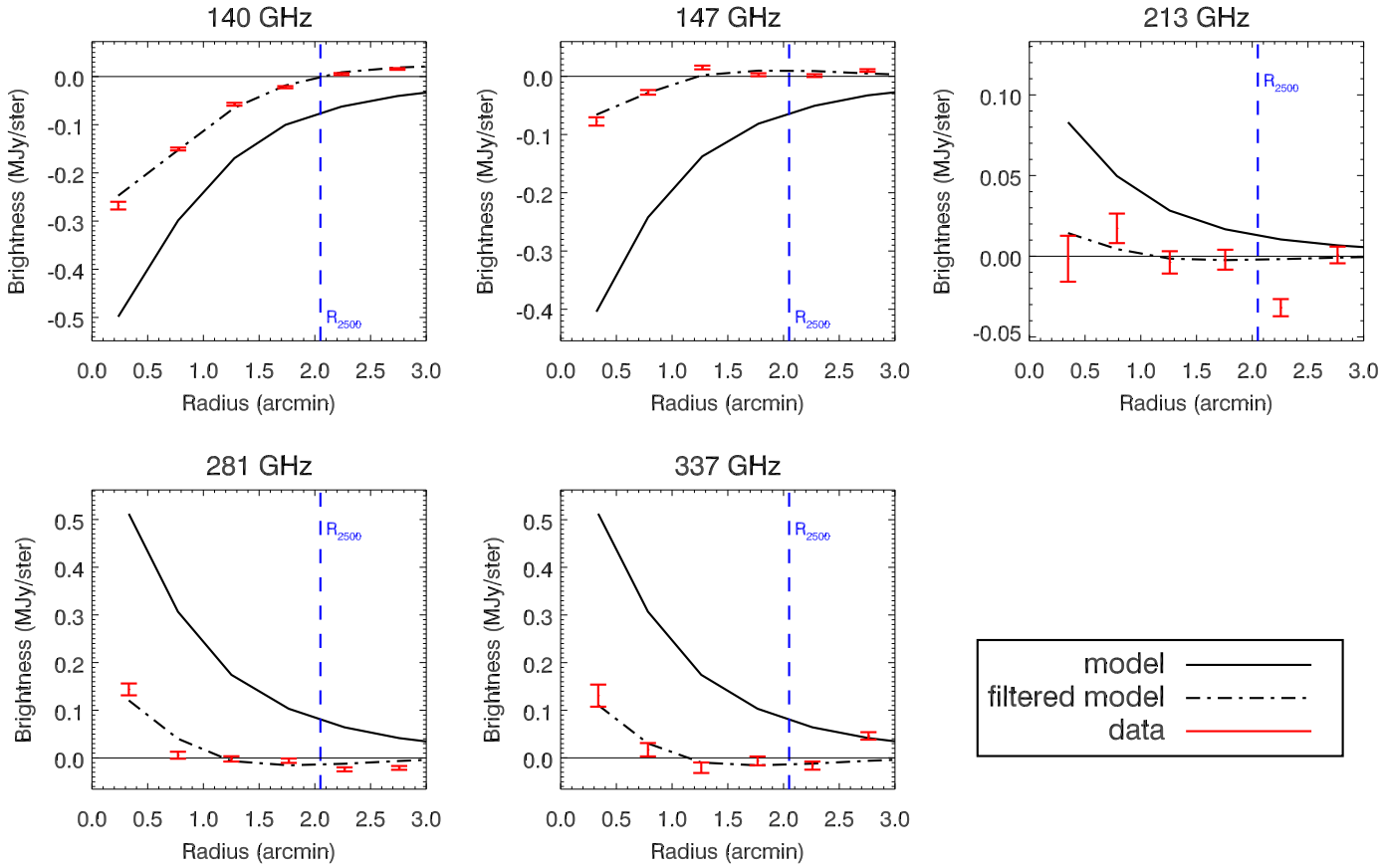

Figure 4. Radial profiles of the SZ data and the elliptical gNFW model used to describe it. In order to compare the model to the data, it must first be convolved with the transfer function of the data processing to determine how it will appear after this filtering. The best-fit model to the data is shown in black, with a solid line representing the model prior to filtering and the dotted–dashed line representing the model after filtering. The filtering attenuates signal on large angular scales, resulting in a peak with a smaller absolute brightness. In addition, the filtered signal passes through zero at intermediate radii, and then takes on the opposite sign at large radii. The data, with error bars, are shown in red and produce a good fit quality to the model in all five bands. The location of R_{2500} is shown as a blue dashed line.

Table 4
SZ Effect Brightness

Band (GHz)	140	147	213	281	337
MJy sr^{-1} $\times$ 10^{-2}	−17.7	−14.3	2.9	18.2	18.2
Covariance (MJy sr^{-1})^2 $\times$ 10^{-4}					
140 GHz	1.3	0.3	0.1	−0.3	0.0
147 GHz	⋯	4.8	0.4	−0.3	−1.5
213 GHz	⋯	⋯	21.7	3.6	7.3
281 GHz	⋯	⋯	⋯	27.9	7.0
337 GHz	⋯	⋯	⋯	⋯	374.4

Note. The average surface brightness within R_{2500} derived from the SZ effect model fits. The top row gives the best fit surface brightness and the bottom set of 5 × 5 entries gives the covariance matrix derived from fits to the 1000 noise realizations.

band correlations are due to the unwanted astrophysical signals and the common planetary calibration model. In addition, primary CMB fluctuations are not a significant noise term in any of the four MUSIC observing bands due to the high-pass filter applied when processing the data, which corresponds to a characteristic angular multipole of $\ell_0 \simeq 7000$–9000 (see Table 1).

A range of other models from the literature were also fit to the data in order to explore how the SZ effect brightness might change as a result of the chosen spatial template of the SZ effect signal. These other models included the average profiles from Arnaud et al. (2010), Planck Collaboration et al. (2013), and Sayers et al. (2013a) along with the RX J1347.5 −1145 specific profile from Bonamente et al. (2012). None of these models produced an acceptable fit quality to the 140 GHz Bolocam data, with probabilities to exceed (PTEs) below 0.001 in all cases.[18] As a result, none of these models are suitable for exploring the model dependence of the results.

[18] The poor fit quality of the ensemble-average profiles from Arnaud et al. (2010), Planck Collaboration et al. (2013), and Sayers et al. (2013a) to the Bolocam data is not surprising, given the large amount of cluster-to-cluster scatter relative to those average profiles. In contrast, and analogous to the nominal Czakon et al. (2015) profile used in this analysis, the Bonamente et al. (2012) profile is based on a fit specifically to RX J1347.5−1145. However, the Bonamente et al. (2012) profile is more centrally peaked than the Czakon et al. (2015) profile, and this difference is the most likely cause of the poor fit quality of the Bonamente et al. (2012) profile to the Bolocam data. The reason for the difference between the profiles derived by Czakon et al. (2015) and Bonamente et al. (2012) is unclear, although several possibilities exist, such as differences in measurement technique, observing frequency, and point-source treatment.

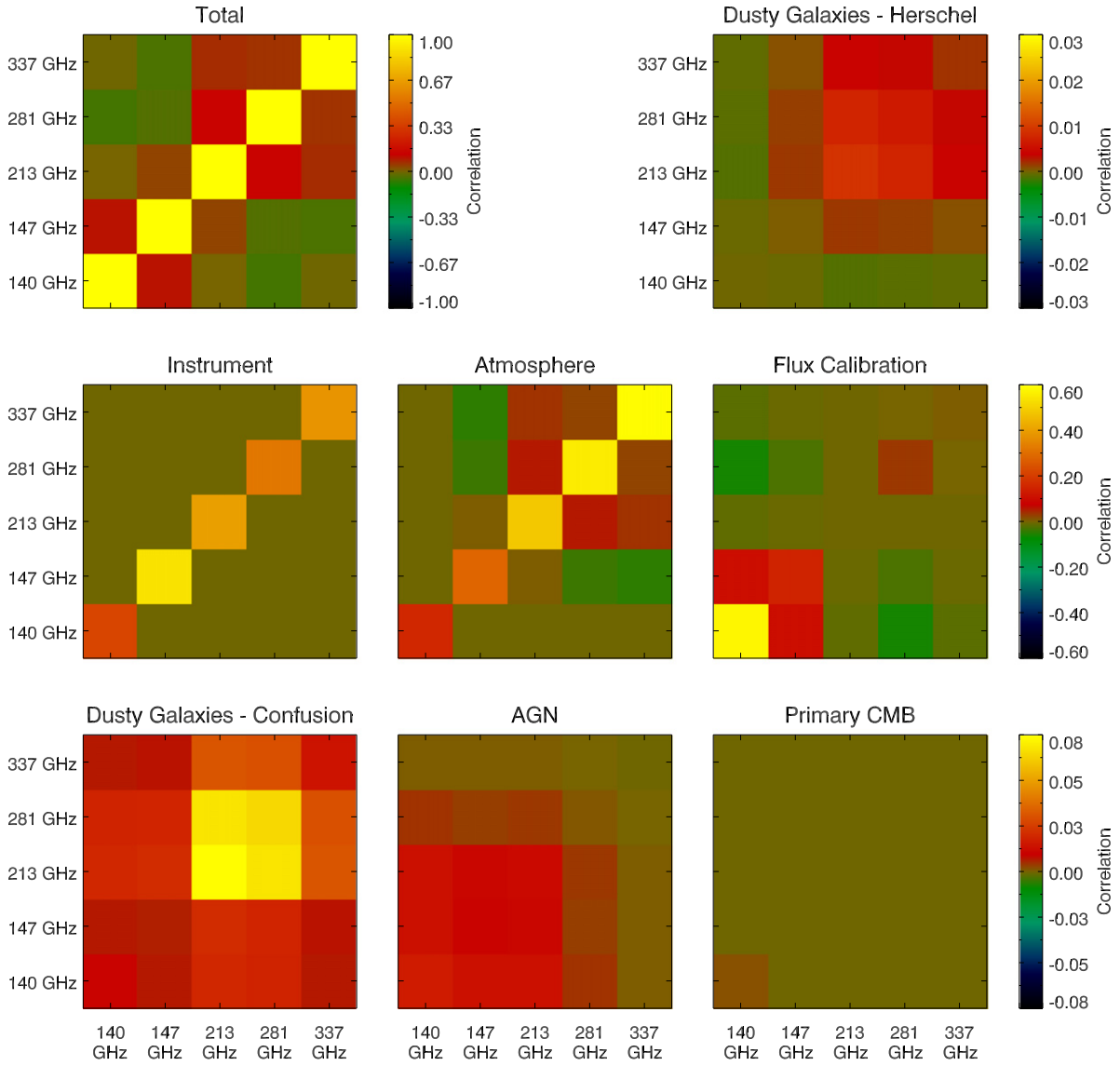

Figure 5. The total covariance matrix is the sum of several noise terms, as described in Section 3.3. To illustrate their relative contribution to the total noise, the plots above show the covariance matrix of each noise term normalized by the diagonal elements of the total covariance matrix. Specifically, $C^{\rm tot} = \sum C^x$ where $C^{\rm tot}$ is the total covariance matrix and C^x is the covariance matrix of noise term x. The plots above show $C^x_{i,j} \Big/ \sqrt{C^{\rm tot}_{i,i} C^{\rm tot}_{j,j}}$, with the total noise covariance (top left), the *Herschel*–SPIRE dusty star-forming galaxy template (top right), noise in the jackknife realizations that is not correlated between image pixels (middle left, approximately equal to the raw photon and instrumental noise), the additional noise in the jackknife realizations that is correlated between image pixels (middle, approximately equal to the residual atmospheric noise), flux calibration uncertainties (middle right), dusty star-forming galaxies below the *Herschel*–SPIRE detection limit (bottom left), uncertainties in the model for the emission from the central AGN (bottom middle), and primary CMB fluctuations (bottom right). Note the different color scales for the three rows. For MUSIC, the effective high-pass filtering of the data processing has a characteristic scale of $\ell_0 \simeq 8000$, and this filter eliminates nearly all of the primary CMB fluctuations.

6. SZ EFFECT SPECTRAL FITS

The total SZ effect brightness can be described according to

$$I(\nu) = I(\nu)_{\rm tSZ} + I(\nu)_{\rm kSZ}$$
$$I(\nu)_{\rm tSZ} = f(\nu, T_{\rm e}) h(\nu) y$$
$$I(\nu)_{\rm kSZ} = -R_{\rm kSZ}(\nu, T_{\rm e}) h(\nu) \frac{v_{\rm pec}}{c} \tau_{\rm e}$$
$$y = \int \frac{k_{\rm B} \sigma_T}{m_{\rm e} c^2} n_{\rm e} T_{\rm e} dl$$
$$\tau_{\rm e} = \int \sigma_T n_{\rm e} dl,$$

where ν is the observing frequency, $k_{\rm B}$ is Boltzmann's constant, σ_T is the Thompson cross section, $m_{\rm e}$ is the electron mass, c is the speed of light, $n_{\rm e}$ and $T_{\rm e}$ are the electron density and temperature, $v_{\rm pec}$ is the ICM line of sight peculiar velocity, $f(\nu, T_{\rm e})$ describes the spectral dependence of the thermal SZ effect signal including relativistic corrections, $h(\nu)$ describes the conversion from a CMB temperature fluctuation to a brightness fluctuation in MJy sr^{-1}, $R_{\rm kSZ}(\nu, T_{\rm e})$ describes the relativistic corrections to the kinetic SZ effect signal, and dl is the differential element along the line of sight. Based on these equations, the total SZ effect signal is dictated by four physical properties of the ICM; $T_{\rm e}$, y, $\tau_{\rm e}$, and $v_{\rm pec}$. Although the five-band

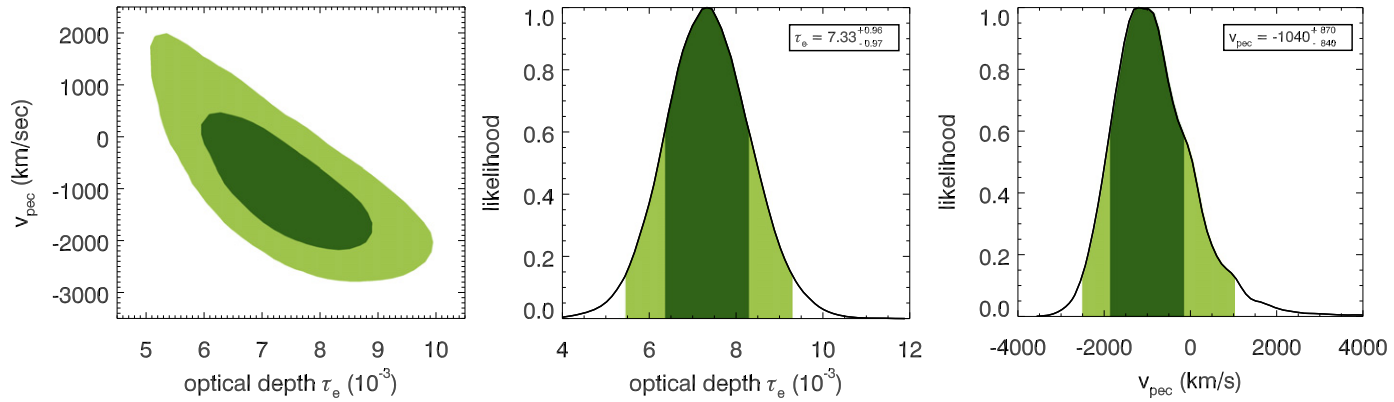

Figure 6. Posterior distributions from the MCMC for the optical depth τ_e and line of sight velocity v_{pec} derived from the five-band SZ effect brightness measurements. Light green indicates the 95% confidence region and dark green indicates the 68% confidence region. The marginalized 68% confidence regions are $\tau_e = 7.33^{+0.96}_{-0.97} \times 10^{-3}$ and $v_{pec} = -1040^{+870}_{-840}$ km s^{-1}.

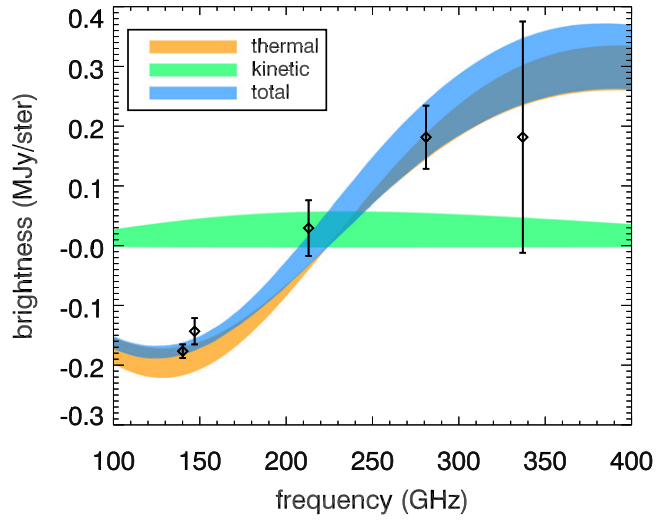

Figure 7. Five-band SZ effect brightness measurements within R_{2500} toward RX J1347.5−1145. The error bars denote the square root of the diagonal elements of the covariance matrix. Overlaid in orange, green, and blue are the 68% confidence regions for the thermal, kinetic, and total SZ effect brightness.

SZ effect brightness measurements described in Section 5 could in principle constrain all four of these ICM properties, a prior for the value of T_e is employed based on the X-ray measurements from *Chandra* described in Section 4. In addition, the ICM is assumed to be isothermal, which implies that $y \propto T_e \tau_e$.

A Markov chain Monte Carlo (MCMC) is employed to sample the parameter space in τ_e and v_{pec} allowed by the five-band SZ effect brightness measurements given in Table 4 along with the X-ray prior on T_e. For each step in the chain, the SZ effect spectrum is computed using the SZpack code described in Chluba et al. (2012, 2013) with the "3D" setting. The results of the MCMC are presented in Figure 6, which shows the clear degeneracy between the values of τ_e and v_{pec}. Separately marginalizing over each parameter yields 68% confidence regions of $\tau_e = 7.33^{+0.96}_{-0.97} \times 10^{-3}$ and $v_{pec} = -1040^{+870}_{-840}$ km s^{-1}. A plot of the 68% confidence regions for the thermal, kinetic, and total SZ effect brightness is shown in Figure 7, with the five-band brightness measurements overlaid.

In order to test the consistency of the SZ effect brightness measurements in the five separate observing bands, along with providing an understanding of the contribution of each observing band to the overall constraints on τ_e and v_{pec}, five additional fits were performed after discarding the data from one of the observing bands. In all cases, the best-fit values of τ_e and v_{pec} shift by less than the 68% uncertainties, and in most cases the shift is much less than the uncertainty value. In addition, the uncertainties on τ_e and v_{pec} generally do not increase significantly when one band is dropped, although dropping the 281 GHz data results in uncertainties that are approximately 50% larger for both τ_e and v_{pec}. This degradation occurs because the 140–213 GHz measurements do not provide a sufficient spectral range to fully disentangle the thermal and kinetic SZ effect signals, and the 337 GHz data exhibit significant noise and do not provide a strong constraint. In addition, removing the 140 GHz Bolocam data, which are approximately two times more sensitive to the SZ effect than the 147 GHz MUSIC data, only results in a $\simeq$15% degradation to the v_{pec} constraint. This is due to the fact that the separation of the thermal and kinetic SZ effect signals is limited almost entirely by the uncertainty on the 281 GHz measurement.

To estimate the systematic uncertainty associated with the X-ray derived value of T_e for RX J1347.5−1145, fits were also performed based on different X-ray analyses. First, if the core region is not excised from the *Chandra* data, then the best-fit value of T_e is 12.7 ± 0.3 keV (compared to 13.4 ± 0.7 keV when the core is excised). This value of T_e results in $\tau_e = 7.52^{+1.04}_{-1.06} \times 10^{-3}$ and $v_{pec} = -740^{+960}_{-970}$ km s^{-1}, which differ by 0.19×10^{-3} and 300 km s^{-1} from the measurements based on a core-excised T_e. An additional fit was also performed using the value of $T_e = 12.1 \pm 0.4$ keV from Mahdavi et al. (2013), which is based on a joint *Chandra*/*XMM* analysis. The best fit values of τ_e and v_{pec} using the Mahdavi et al. (2013) measurement are $7.89^{+1.01}_{-1.02} \times 10^{-3}$ and -770^{+800}_{-800} km s^{-1}, which differ by 0.56×10^{-3} and 270 km s^{-1} from the values obtained using the nominal measurement of T_e. Compared to the measurement uncertainties, the differences due to the X-ray analysis are smaller by a factor of approximately two for τ_e and by a factor of approximately three for v_{pec}, indicating that the range of values for T_e obtained from different analyses does not significantly change the derived ICM constraints, particularly for v_{pec}.

In addition, to determine the effect of assuming an isothermal ICM, rather than a multi-temperature ICM, a fit was performed based on the measurements presented in

Table 5
ICM Optical Depth and Velocity Constraints

140 GHz	147 GHz	213 GHz	281 GHz	337 GHz	τ_e 10^{-3}	v_{pec} km s^{-1}
✓	✓	✓	✓	✓	$7.33^{+0.96}_{-0.97}$	-1040^{+870}_{-840}
	✓	✓	✓	✓	$6.41^{+1.12}_{-1.13}$	-1300^{+1110}_{-1080}
✓	…	✓	✓	✓	$7.34^{+0.95}_{-0.95}$	-890^{+890}_{-870}
✓	✓	…	✓	✓	$7.14^{+0.98}_{-0.97}$	-870^{+960}_{-920}
✓	✓	✓	…	✓	$7.87^{+1.64}_{-1.57}$	-1730^{+1440}_{-1180}
✓	✓	✓	✓	…	$7.40^{+1.04}_{-1.05}$	-1130^{+940}_{-930}

Note. Marginalized 68% confidence regions for τ_e and v_{pec} based on fits to the full data set (top row) and to subsets of the data. The check marks indicate which observing bands were included in the fit. Removing the data from one observing band does not cause the best-fit values to move outside of the 68% confidence regions, although the uncertainties become significantly larger when the 281 GHz band is excluded. Due to the relatively high noise in the 337 GHz band, removing the 281 GHz band significantly reduces the spectral coverage of the data and makes it more difficult to separate the thermal and kinetic SZ effect signals.

Johnson et al. (2012). Specifically, they find two hot regions within the ICM with $T_e \simeq 25 \pm 5$ keV. Based on the high-resolution SZ effect results presented in Mason et al. (2010), these hotter regions are likely to contribute $\lesssim$10% of the total SZ effect signal. If 90% of the ICM is assumed to have $T_e = 13.4 \pm 0.7$ keV, and 10% is assumed to have $T_e = 25 \pm 5$ keV, then the best fit values of τ_e and v_{pec} are $6.55^{+0.87}_{-0.85} \times 10^{-3}$ and -1140^{+1060}_{-900} km s^{-1}, which differ by 0.78×10^{-3} and 100 km s^{-1} from the values obtained in the nominal isothermal fit. Particularly for v_{pec}, these differences are smaller than the measurement uncertainties, and indicate that the isothermal ICM assumption does not have a strong effect on the derived τ_e and v_{pec} constraints.

As described in Section 3.2, a wide range of lower frequency observations were used to model the emission from the central AGN and to subtract it from the Bolocam+MUSIC data. To estimate the potential impact of the AGN emission on the final results, a fit was performed without the AGN subtracted from the Bolocam+MUSIC images. The associated best-fit values of τ_e and v_{pec} are $7.39^{+1.03}_{-1.02} \times 10^{-3}$ and -1910^{+840}_{-840} km s^{-1}, which differ from the nominal best-fit values by 0.06×10^{-3} and 870 km s^{-1}. In the case of v_{pec}, this difference is significant, and indicates that the potential bias from the AGN emission is comparable to the measurement uncertainties. Analogously, a fit was performed without subtracting the *Herschel*–SPIRE-derived model of the dusty star-forming galaxies, and the best-fit values of τ_e and v_{pec} from this fit are $6.91^{+1.02}_{-1.04} \times 10^{-3}$ and -560^{+900}_{-890} km s^{-1}. These differ from the nominal best-fit values by 0.42×10^{-3} and 480 km s^{-1}, and indicate that the potential v_{pec} bias from the dusty star-forming galaxy emission is approximately 2 times lower than the potential bias from the AGN emission while the potential τ_e bias is larger.

7. COMPARISON TO PREVIOUS RESULTS

Our derived $v_{pec} = -1040^{+870}_{-840}$ km s^{-1} is in good agreement with the previously published kinetic SZ effect value of $v_{pec} = -1420^{+1270}_{-1170}$ km s^{-1} from Kitayama et al. (2004). Furthermore, both of these measurements are consistent with the expected distribution of the bulk component of v_{pec} for massive clusters, which has an rms of ~200–300 km s^{-1}(e.g., Hernández-Monteagudo & Sunyaev 2010). However, both results are noticeably offset from the value of $v_{pec} = +450 \pm 810$ km s^{-1} derived in the kinetic SZ analysis of Zemcov et al. (2012), although there are a number of systematic differences in measurement technique that could explain this difference. The Zemcov et al. (2012) measurement was made using the single-beam Z-Spec instrument and was therefore only sensitive to the value of v_{pec} within a $\simeq$30″ diameter region near the cluster center (compared to the more extended bulk cluster measurements in Kitayama et al. (2004) and in this work). In relatively small regions of the ICM, similar to what was probed in the Zemcov et al. (2012) analysis, the internal ICM motions can be significant ($\simeq$500 km s^{-1}, e.g., Nagai et al. 2003; Dolag & Sunyaev 2013), and such motions could easily reconcile the results. In particular, merger activity near the center of RX J1347.5−1145, for which evidence is seen by Mason et al. (2010), Johnson et al. (2012), and Kreisch et al. (2014), could potentially source such large internal motions in that region.

Our derived $\tau_e = 7.39^{+1.03}_{-1.02} \times 10^{-3}$, which gives the mean line of sight integrated electron optical depth within the plane-of-sky aperture R_{2500}, can be used to obtain a constraint on the gas mass (M_{gas}) of RX J1347.5−1145. First, the parametric model given in Section 5 is used to convert between τ_e and $\tau_{e,sphere} = 5.48 \pm 0.77 \times 10^{-3}$, where $\tau_{e,sphere}$ represents the mean optical depth integrated within the line of sight defined by R_{2500} and the small asymmetry in the uncertainties on τ_e is neglected. The gas mass can then be determined according to

$$M_{gas} = \left(\frac{\tau_{e,sphere}}{\sigma_T}\right)(\pi R_{2500}^2)(\mu_e m_p),$$

where $\mu_e = 1.14$ is the mean molecular weight per free electron and m_p is the proton mass, yielding $M_{gas} = 11.9 \pm 1.7 \times 10^{13}$ $M_\odot$. We compare our SZ-derived M_{gas} to prior X-ray-derived M_{gas} values in Table 6, including the value of M_{gas} found by Czakon et al. (2015) as part of their X-ray analysis to define the value of R_{2500} used throughout this manuscript. In each case, the SZ estimation of M_{gas} was made using the R_{2500} value obtained by the indicated X-ray analysis. The prior on T_e was kept at its nominal value, as small changes in aperture have a negligible effect on T_e relative to its uncertainty.

This comparison indicates that, on average, the analyses incorporating SZ data yield systematically higher values of M_{gas} than the X-ray-only analyses. Such a difference could easily be explained by an elongation of the cluster along the line of sight, which would boost the SZ signal compared to the X-ray signal (e.g., Morandi et al. 2012). This result is in good agreement with Pointecouteau et al. (2001) and Kitayama et al. (2004), who also find a slight preference for line of sight elongation based on an SZ/X-ray comparison. In contrast, Chakrabarty et al. (2008), Bonamente et al. (2012), and Plagge et al. (2013) all find significantly lower SZ signals for RX J1347.5−1145 than expected from the X-ray data, and those analyses imply a line of sight compression with axial ratios ranging from ~3–5. The reason for the disagreement between these two sets of results is not clear, although it may be related to differences in the SZ data. For example, Pointecouteau et al. (2001), Kitayama et al. (2004), and this work use bolometric imaging data at mm wavelengths while Chakrabarty et al. (2008), Bonamente et al. (2012), and Plagge et al. (2013) use interferometric data at centimeter wavelengths.

Table 6
SZ and X-Ray Derived M_{gas}

X-Ray Analysis	R_{2500} (Mpc)	X-ray M_{gas} ($10^{13} M_{\odot}$)	SZ M_{gas} ($10^{13} M_{\odot}$)
Czakon et al. (2015)	0.71	9.2 ± 1.0	11.9 ± 1.7
Donahue et al. (2014)	0.74	9.5 ± 0.5	11.7 ± 1.8
Mantz et al. (2014)	0.80	13.6 ± 1.5	13.1 ± 1.8

Note. Comparison of M_{gas} values obtained from three prior X-ray-only analyses to that obtained from this analysis incorporating SZ data. For each comparison, the SZ analysis is redone using the indicated X-ray-derived value of R_{2500}, though with a common T_e prior as described in Section 4. As noted in the text, variations in T_e due to these small changes in aperture are negligible compared to the measurement uncertainty on T_e. For both the Czakon et al. (2015) and Donahue et al. (2014) comparisons, the SZ data find a value of M_{gas} that is approximately 2σ larger than the X-ray value, while the agreement is good in the case of the Mantz et al. (2014) comparison.

In addition, all six SZ data sets have sensitivities to different angular scales. Furthermore, the techniques used to fit the SZ and X-ray data, and to compare them, are different in all six of the analyses. Resolving these discrepancies is beyond the scope of this work and will likely require a dedicated, uniform re-analysis of all the relevant data.

8. SUMMARY

By combining four-band MUSIC images with a 140 GHz Bolocam image we have constrained the thermal and kinetic SZ effect signals toward RX J1347.5−1145. Based on these constraints, and including a prior on the ICM temperature derived from X-ray spectroscopic measurements from *Chandra*, we find $v_{pec} = -1040^{+870}_{-840}\,\mathrm{km\,s^{-1}}$. This value is in good agreement with the previously published result from Kitayama et al. (2004), but is in mild tension with the velocity found by Zemcov et al. (2012). However, some or all of that tension may be due to internal cluster motions within the relatively small cluster volume sampled by Zemcov et al. (2012). We find a mean electron optical depth within R_{2500} of $\tau_e = 7.39^{+1.03}_{-1.02} \times 10^{-3}$, which implies a gas mass within R_{2500} of $M_{gas} = 11.9 \pm 1.7 \times 10^{13}\,M_{\odot}$. This mass is slightly higher than previous values of M_{gas} derived from X-ray analyses, implying a slight elongation of RX J1347.5−1145 along the line of sight.

For this analysis, we have included a rigorous treatment of the photon and instrumental noise, noise due to fluctuations in the atmospheric brightness, uncertainties in the planetary flux calibration model, and noise from three unwanted astrophysical sources (primary CMB fluctuations, dusty star-forming galaxies, and the cluster's central AGN). In the case of the dusty star-forming galaxies, we have used data from *Herschel*–SPIRE to subtract the brightest objects. Most of the noise sources are correlated between the five observing bands, and all of these covariances have been accounted for in our overall results. For the four MUSIC bands, the total noise is largely due to the combination of photon, instrumental, and atmospheric noise, which implies that longer integration times would yield significantly better constraints. For example, if we eliminate these noise sources from our analysis, then the uncertainties on τ_e and v_{pec} are reduced by approximately a factor of two to $\pm 0.44 \times 10^{-3}$ and $\pm 460\,\mathrm{km\,s^{-1}}$, respectively. In addition, more advanced data-processing algorithms to remove the atmospheric fluctuations that are correlated between the four MUSIC observing bands may produce noticeable improvements (Benson et al. 2003; Adam et al. 2014).

We thank the anonymous referee for his or her extensive suggestions to improve this manuscript. We acknowledge the assistance of: the day crew and Hilo staff of the Caltech Submillimeter Observatory, who provided invaluable assistance during data-taking for this data set; Kathy Deniston and Diana Bisel, who provided effective administrative support at Caltech and in Hilo; J.S. was partially supported by a Norris Foundation Fellowship; N.G.C. was partially supported by a NASA Graduate Student Research Fellowship; S.R.S. was supported by a NASA Earth and Space Science Fellowship; MUSIC was constructed and commissioned with funding provided by the Gordon and Betty Moore Foundation, JPL internal funds, and the NSF Advanced Technologies and Instrumentation (ATI) and Astronomy and Astrophysics Grants (AAG) Programs. This work is based in part on observations made with *Herschel*, a European Space Agency Cornerstone Mission with a significant participation by NASA. Partial support for this work was provided by NASA through an award issued by JPL/Caltech. This research was performed while TM held a National Research Council Research Associateship Award at the Naval Research Laboratory.

Facilities: CSO, *Chandra*, *Herschel*.

REFERENCES

Adam, R., Comis, B., Macías-Pérez, J. F., et al. 2014, A&A, 569, A66
Adam, R., Comis, B., Macías-Pérez, J.-F., et al. 2015, A&A, 576, A12
Arnaud, M., Pratt, G. W., Piffaretti, R., et al. 2010, A&A, 517, A92
Benson, B. A., Church, S. E., Ade, P. A. R., et al. 2003, ApJ, 592, 674
Béthermin, M., Dole, H., Lagache, G., Le Borgne, D., & Penin, A. 2011, A&A, 529, A4
Bhattacharya, S., & Kosowsky, A. 2008, PhRvD, 77, 083004
Birkinshaw, M. 1999, PhR, 310, 97
Bonamente, M., Hasler, N., Bulbul, E., et al. 2012, NJPh, 14, 025010
Carlstrom, J. E., Holder, G. P., & Reese, E. D. 2002, ARA&A, 40, 643
Chakrabarty, D., de Filippis, E., & Russell, H. 2008, A&A, 487, 75
Chluba, J., Nagai, D., Sazonov, S., & Nelson, K. 2012, MNRAS, 426, 510
Chluba, J., Switzer, E., Nelson, K., & Nagai, D. 2013, MNRAS, 430, 3054
Clarkson, C. 2012, CRPhy, 13, 682
Clarkson, C., Bassett, B., & Lu, T. H.-C. 2008, PhRvL, 101, 011301
Coble, K., Bonamente, M., Carlstrom, J. E., et al. 2007, AJ, 134, 897
Condon, J. J., Cotton, W. D., Greisen, E. W., et al. 1998, AJ, 115, 1693
Czakon, N. G., Sayers, J., Mantz, A., et al. 2015, ApJ, 806, 18
Dolag, K., & Sunyaev, R. 2013, MNRAS, 432, 1600
Donahue, M., Voit, G. M., Mahdavi, A., et al. 2014, ApJ, 794, 136
Duan, R. 2015, PhD thesis, Caltech
Duan, R., McHugh, S., Serfass, B., et al. 2010, Proc. SPIE, 7741, 1
George, E. M., Reichardt, C. L., Aird, K. A., et al. 2015, ApJ, 799, 177
Glenn, J., Bock, J. J., Chattopadhyay, G., et al. 1998, Proc. SPIE, 3357, 326
Glenn, J., Day, P. K., Ferry, M., et al. 2008, Proc. SPIE, 7020, 0
Goldin, A., Bock, J. J., Hunt, C. L., et al. 2003, Proc. SPIE, 4855, 163
Golwala, S. R., Bockstiegel, C., Brugger, S., et al. 2012, Proc. SPIE, 8452, 5
Haig, D. J., Ade, P. A. R., Aguirre, J. E., et al. 2004, Proc. SPIE, 5498, 78
Hand, N., Addison, G. E., Aubourg, E., et al. 2012, PhRvL, 109, 041101

Hernández-Monteagudo, C., & Sunyaev, R. A. 2010, A&A, 509, A82
Johnson, R. E., Zuhone, J., Jones, C., Forman, W. R., & Markevitch, M. 2012, ApJ, 751, 95
Kaiser, N. 1987, MNRAS, 227, 1
Kashlinsky, A., Atrio-Barandela, F., Kocevski, D., & Ebeling, H. 2008, ApJL, 686, L49
Kelly, B. C. 2007, ApJ, 665, 1489
Kitayama, T., Komatsu, E., Ota, N., et al. 2004, PASJ, 56, 17
Komatsu, E., Kitayama, T., Suto, Y., et al. 1999, ApJL, 516, L1
Komatsu, E., Matsuo, H., Kitayama, T., et al. 2001, PASJ, 53, 57
Korngut, P. M., Dicker, S. R., Reese, E. D., et al. 2011, ApJ, 734, 10
Kosowsky, A., & Bhattacharya, S. 2009, PhRvD, 80, 062003
Kreisch, C., Machacek, M. E., Randall, S. W., & Jones, C. 2014, in American Astronomical Society Meeting Abstracts, 223, 358
Kumar, S., Vayonakis, A., LeDuc, H. G., et al. 2009, ITAS, 19, 924
Lindner, R. R., Aguirre, P., Baker, A. J., et al. 2015, ApJ, 803, 79
Mahdavi, A., Hoekstra, H., Babul, A., et al. 2013, ApJ, 767, 116
Maloney, P. R., Czakon, N. G., Day, P. K., et al. 2010, Proc. SPIE, 7741, 0
Mantz, A., Allen, S. W., Ebeling, H., Rapetti, D., & Drlica-Wagner, A. 2010, MNRAS, 406, 1773
Mantz, A. B., Allen, S. W., Morris, R. G., et al. 2014, MNRAS, 440, 2077
Mantz, A. B., Allen, S. W., Morris, R. G., et al. 2015, MNRAS, 449, 199
Mason, B. S., Dicker, S. R., Korngut, P. M., et al. 2010, ApJ, 716, 739
Mauskopf, P. D., Horner, P. F., Aguirre, J., et al. 2012, MNRAS, 421, 224
Morandi, A., Limousin, M., Sayers, J., et al. 2012, MNRAS, 425, 2069
Mroczkowski, T., Dicker, S., Sayers, J., et al. 2012, ApJ, 761, 47
Nagai, D., Kravtsov, A. V., & Kosowsky, A. 2003, ApJ, 587, 524
Nagai, D., Kravtsov, A. V., & Vikhlinin, A. 2007, ApJ, 668, 1
Osborne, S. J., Mak, D. S. Y., Church, S. E., & Pierpaoli, E. 2011, ApJ, 737, 98
Plagge, T. J., Marrone, D. P., Abdulla, Z., et al. 2013, ApJ, 770, 112
Planks Collaboration, Ade, P. A. R., Aghanim, N., et al. 2013, A&A, 550, A131
Planks Collaboration, Ade, P. A. R., Aghanim, N., et al. 2014, A&A, 561, A97
Planck Collaboration, Ade, P. A. R., Aghanim, N., et al. 2015a, arXiv:1507.02704
Planck Collaboration, Aghanim, N., Arnaud, M., et al. 2015b, arXiv:1504.03339
Pointecouteau, E., Giard, M., Benoit, A., et al. 1999, ApJL, 519, L115
Pointecouteau, E., Giard, M., Benoit, A., et al. 2001, ApJ, 552, 42
Reese, E. D., Carlstrom, J. E., Joy, M., et al. 2002, ApJ, 581, 53
Sayers, J., Bockstiegel, C., Brugger, S., et al. 2014, Proc. SPIE, 9153, 4
Sayers, J., Czakon, N. G., & Golwala, S. R. 2012, ApJ, 744, 169
Sayers, J., Czakon, N. G., Mantz, A., et al. 2013b, ApJ, 764, 152
Sayers, J., Golwala, S. R., Ameglio, S., & Pierpaoli, E. 2011, ApJ, 728, 39
Sayers, J., Mroczkowski, T., Czakon, N. G., et al. 2013c, ApJ, 778, 52
Sayers, J., Mroczkowski, T., Zemcov, M., et al. 2013a, ApJ, 768, 177
Scoccimarro, R. 2004, PhRvD, 70, 083007
Sievers, J. L., Hlozek, R. A., Nolta, M. R., et al. 2013, JCAP, 10, 60
Sunyaev, R. A., & Zel'dovich, Y. B. 1972, CoASP, 4, 173
Sunyaev, R. A., & Zeldovich, I. B. 1980, MNRAS, 190, 413
Zemcov, M., Aguirre, J., Bock, J., et al. 2012, ApJ, 749, 114